

Magnetorotational dynamo chimeras

The missing link to turbulent accretion disk dynamo models?

A. Riols¹, F. Rincon^{2,3}, C. Cossu⁴, G. Lesur^{5,6}, G. I. Ogilvie¹, and P-Y. Longaretti^{5,6}

¹ Department of Applied Mathematics and Theoretical Physics, University of Cambridge, Centre for Mathematical Sciences, Wilberforce Road, Cambridge CB3 0WA, UK e-mail: ar764@cam.ac.uk

² Université de Toulouse; UPS-OMP, IRAP Toulouse, France e-mail: francois.rincon@irap.omp.eu

³ CNRS, IRAP, 14 avenue Edouard Belin, 31400 Toulouse, France

⁴ Institut de Mécanique des Fluides de Toulouse (IMFT), CNRS – Université de Toulouse, Allée du Pr. Camille Soula, 31400 Toulouse, France

⁵ CNRS, IPAG, 38000 Grenoble, France

⁶ Univ. Grenoble Alpes; IPAG, 38000 Grenoble, France

July 12, 2016

ABSTRACT

In Keplerian accretion disks, turbulence and magnetic fields may be jointly excited through a subcritical dynamo process involving the magnetorotational instability (MRI). High-resolution simulations exhibit a tendency towards statistical self-organization of MRI dynamo turbulence into large-scale cyclic dynamics. Understanding the physical origin of these structures, and whether they can be sustained and transport angular momentum efficiently in astrophysical conditions, represents a significant theoretical challenge. The discovery of simple periodic nonlinear MRI dynamo solutions has recently proven useful in this respect, and has notably served to highlight the role of turbulent magnetic diffusion in the seeming decay of the dynamics at low magnetic Prandtl number Pm (magnetic diffusivity larger than viscosity), a common regime in accretion disks. The connection between these simple structures and the statistical organization reported in turbulent simulations remained elusive, though. Here, we report the numerical discovery in moderate aspect ratio Keplerian shearing boxes of new periodic, incompressible, three-dimensional nonlinear MRI dynamo solutions with a larger dynamical complexity reminiscent of such simulations. These “chimera” cycles are characterized by multiple MRI-unstable dynamical stages, but their basic physical principles of self-sustainment are nevertheless identical to those of simpler cycles found in azimuthally elongated boxes. In particular, we find that they are not sustained at low Pm either due to subcritical turbulent magnetic diffusion. These solutions offer a new perspective into the transition from laminar to turbulent instability-driven dynamos, and may prove useful to devise improved statistical models of turbulent accretion disk dynamos.

Key words. accretion, accretion disks – dynamo – instabilities – magnetohydrodynamics (MHD) – turbulence

1. Introduction

The magnetorotational instability (MRI) is considered one of the main sources of angular momentum-transporting turbulence in astrophysical accretion disks. It requires a magnetic field and a differentially rotating flow whose angular velocity decreases with distance to the rotation axis (Velikhov 1959; Chandrasekhar 1960; Balbus & Hawley 1991). Numerical studies have shown that in the presence of a constant net vertical magnetic flux, the MRI acts as a powerful linear instability which amplifies arbitrarily small perturbations that break down nonlinearly into MHD turbulence (Hawley et al. 1995; Stone et al. 1996). The efficiency of the turbulence at transporting angular momentum, however, remains a matter of debate and may depend on dissipative processes. This transport may notably be limited in the astrophysically relevant regime of low magnetic Prandtl number (Pm), where Pm denotes the ratio between the kinematic viscosity and magnetic diffusivity of the fluid (Lesur & Longaretti 2007; Balbus & Henri 2008; Meheut et al. 2015).

A distinct but related problem is the origin of the magnetic field that supports the MRI in such astrophysical systems. In the absence of an externally imposed field, one possibility is that the field is created and sustained inside the disk by a turbulent dy-

namo process. A good candidate is the so-called subcritical MRI dynamo process, by which magnetohydrodynamic (MHD) perturbations excited by the MRI nonlinearly sustain the large scale field that made the instability possible in the first place (Hawley et al. 1995, 1996; Rincon et al. 2007; Lesur & Ogilvie 2008a; Rincon et al. 2008). Simulations of “zero net magnetic flux” configurations have shown that this process can self-sustain and lead to MHD turbulence that transports significant angular momentum. Many simulations of MRI dynamo turbulence also exhibit self-organized large-scale dynamics characterised by chaotic reversals of the large-scale magnetic field, somewhat reminiscent of the “butterfly” diagram of the solar dynamo (Brandenburg et al. 1995; Davis et al. 2010; Simon et al. 2011; Gressel & Pessah 2015). The viability of an MRI dynamo process in disks remains unclear though, as numerical studies explicitly taking into account dissipative process suggest that it cannot be sustained for $Pm \lesssim 1$ (Fromang et al. 2007). The highest-resolution incompressible simulations to date indicate that no MRI dynamo can be excited at $Pm = 1$ for magnetic Reynolds numbers (Rm) as large as $Rm = 45000$ (Walker et al. 2016), but other studies have found some dependence of this effect on geometry and stratification (Oishi & Mac Low 2011; Shi et al. 2016).

A fundamental physical understanding of the different processes at work in the subcritical MRI dynamo appears to be required to make sense of these different numerical observations. Simple three-dimensional nonlinear periodic dynamo solutions of the MHD equations (Herauld et al. 2011, hereafter H11) have recently been shown to provide the first germs of nonlinear MRI dynamo excitation in the Keplerian differential rotation regime in azimuthally elongated shearing box numerical configurations at transitional kinematic (Re) and magnetic Reynolds numbers (Riols et al. 2013, hereafter R13). These solutions represent an interesting avenue of research to investigate the inner workings and transitional properties of this dynamo. A recent analysis of the energy budget of a few such cycles has notably proven useful to pinpoint the possible role of a “subcritical” turbulent magnetic diffusion in the seeming decay of the dynamics at low Pm (Riols et al. 2015, hereafter R15).

One possible caveat with this approach so far, though, has been the difficulty to connect these fairly ordered (yet fully three-dimensional and nonlinear) periodic solutions to developed turbulent MHD states produced in generic moderate aspect ratio simulations at larger Re and Rm, and in particular to statistically self-organized MRI dynamo butterflies. The aim of this paper is to bridge part of this gap by presenting several new three-dimensional nonlinear periodic MRI dynamo solutions computed in moderate aspect ratio shearing boxes. As we shall see, the dynamical complexity of these cycles, which we call “MRI dynamo chimeras” because they involve multiple MRI-unstable dynamical stages, is significantly larger than that of the simpler solutions discussed previously, and is reminiscent of the statistical behaviour observed in generic numerical simulations. Yet, their sustainment rests on the exact same few linear and nonlinear dynamical processes underlying the dynamics of simpler cycles.

The mathematical and numerical frameworks of our study are presented in Sect. 2, which also provides a discussion of the effects of changing the aspect ratio in this problem. Section 3 documents the dynamical properties of two new pairs of dynamically complex chimera MRI dynamo cycles computed in moderate aspect ratio configurations with a Newton-Krylov algorithm, and shows that their existence is limited to Pm larger than a few. Section 4 extends the magnetic energy budget analysis of R15 to these structures, and shows that the enhancement of nonlinear transfers of magnetic energy to small scales at large Re (“subcritical turbulent magnetic diffusion”) prevents the sustainment of these structures at lower Pm, just as in the case of simpler cycles. In Sect. 5, we discuss the semi-statistical nature of these new cycles and the perspectives that their computation opens for the development of improved statistical models of Keplerian dynamos, and more generally instability-driven dynamos. A summary of the main conclusions and short discussion of how the results may fit into the wider astrophysical context concludes the paper.

2. Equations and numerical framework

2.1. Model

The equations and numerical frameworks have been described extensively in R13. We only recall the essential points here. We use the cartesian local shearing sheet description of differentially rotating flows (Goldreich & Lynden-Bell 1965), whereby the axisymmetric differential rotation is approximated locally by a linear shear flow $\mathbf{U}_x = -Sx\mathbf{e}_y$, and a uniform rotation rate $\boldsymbol{\Omega} = \Omega\mathbf{e}_z$, with $\Omega = 2/3S$ for a Keplerian shear flow. Here

(x, y, z) are respectively the shearwise, streamwise and spanwise directions, corresponding to the radial, azimuthal and vertical directions in accretion disks. We refer to the (x, z) projection of vector fields as their poloidal components and to the y direction as their toroidal (azimuthal) one. We ignore stratification and compressible effects. The evolution of the three-dimensional velocity field perturbations \mathbf{u} and magnetic field \mathbf{B} is governed by the three-dimensional incompressible, dissipative MHD equations:

$$\nabla \cdot \mathbf{u} = 0, \quad \nabla \cdot \mathbf{B} = 0. \quad (1)$$

$$\frac{\partial \mathbf{u}}{\partial t} - Sx \frac{\partial \mathbf{u}}{\partial y} + \mathbf{u} \cdot \nabla \mathbf{u} = -2\boldsymbol{\Omega} \times \mathbf{u} + S u_x \mathbf{e}_y - \nabla \Pi + \mathbf{B} \cdot \nabla \mathbf{B} + \nu \Delta \mathbf{u}, \quad (2)$$

$$\frac{\partial \mathbf{B}}{\partial t} - Sx \frac{\partial \mathbf{B}}{\partial y} = -S B_x \mathbf{e}_y + \nabla \times (\mathbf{u} \times \mathbf{B}) + \eta \Delta \mathbf{B}. \quad (3)$$

where Π is the sum of the gas and magnetic pressure. The density is fixed to $\rho = 1$. The kinematic and magnetic Reynolds numbers are defined by $\text{Re} = SL^2/\nu$ and $\text{Rm} = SL^2/\eta$, where ν and η are the constant kinematic viscosity and magnetic diffusivity, L is a typical scale of the spatial domain and time is measured with respect to S^{-1} . The magnetic Prandtl number is $\text{Pm} = \nu/\eta = \text{Rm}/\text{Re}$. \mathbf{B} is expressed in terms of an alfvénic velocity. Both \mathbf{u} and \mathbf{B} are measured in units of SL .

2.2. Numerical methods

We use the SNOOPY code (Lesur & Longaretti 2007) to perform direct numerical simulations (DNS) of Eqs. (1)-(3). This code provides a spectral implementation of the so-called numerical shearing box model of the shearing sheet, in a finite domain of size (L_x, L_y, L_z) , at numerical resolution (N_x, N_y, N_z) . The x and y directions are taken as periodic while shear-periodicity is imposed in x . As the box is shear-periodic, any numerical solution can be decomposed into a set of shearing Fourier modes with wavenumbers

$$k_x(t) = -\ell k_{x_0} + m k_{y_0} t, \quad k_y = m k_{y_0} \quad \text{and} \quad k_z = n k_{z_0}, \quad (4)$$

where $k_{x_0} = 2\pi/L_x$, $k_{y_0} = 2\pi/L_y$, $k_{z_0} = 2\pi/L_z$ (a detailed description of the spectral decomposition used in the simulations is provided in R13). A shearing wave is a non-axisymmetric wave with $m \neq 0$. Because of the shear-periodicity in x , the radial Eulerian wavenumber k_x of a given shearing wave increases linearly in time (ℓ is the corresponding integer Lagrangian wavenumber). The wave is “leading” when $k_x k_y < 0$ and “trailing” when $k_x k_y > 0$.

Nonlinear periodic solutions are computed with the Newton-Krylov solver PEANUTS (see again R13) interfaced to SNOOPY, and followed in parameter space using arclength continuation. We enforce that the dynamics takes place in a symmetric subspace to facilitate the analysis (this does not compromise the underlying dynamical complexity), and notably monitor the axisymmetric MRI-supporting field $\bar{\mathbf{B}}$ ($(x-y)$ average of \mathbf{B}), more specifically its energetically dominant Fourier mode $\bar{\mathbf{B}}_0(z, t) = \bar{\mathbf{B}}_0(t) \cos(k_{z_0} z)$.

2.3. Large vs moderate aspect ratio

In H11, R13 and R15, the nonlinear dynamics was restricted to elongated boxes in the azimuthal direction with typical azimuthal to radial aspect ratio $L_y/L_x \sim 30$. The main reason for this choice was to simplify the dynamics as much as possible and reduce the number of coexisting cyclic solutions. Indeed, at low Re and Rm (defined on $L_x \sim L_z$) and $L_y/L_x \gg 1$ the dynamics in the (L_x, L_z) plane remains quite laminar but the dissipation of non-axisymmetric structures is sufficiently small that (just a few) weakly nonlinear three-dimensional structures can be sustained. H11 showed that the sustainment of these large-aspect ratio cycles can be understood in generic physical terms involving shearing effects, the linear physics of non-axisymmetric MRI-unstable perturbations, and nonlinear feedback mechanisms. One may nevertheless argue that large-aspect ratio configurations are somewhat unnatural, and indeed the connection with turbulent MRI dynamo simulations conducted at moderate aspect ratio does not seem straightforward.

Here, we therefore attempt to extend this “cycle hunt” to moderate aspect ratios, down to $L_y/L_x \sim 4$. Because k_{y0} is larger in this configuration, non-axisymmetric shearing waves are sheared out and dissipated faster for a given set of Re and Rm (once again defined on $L_x \sim L_z$). Hence, one has to go to larger Re and Rm (typically $Rm \sim 3000$ for $L_y/L_x \sim 4$) to recover the first germs of sustained (recurrent) MRI dynamo activity. However, doing so also implies that the dynamics in the (L_x, L_z) plane is more complex than in the large aspect ratio case because of the larger available number of poloidal dynamical degrees of freedom. The two main consequences, from the perspective of capturing nonlinear solutions, are that a larger number of them coexist in the phase space of the problem for a given Re and Rm, making it more difficult to converge on any of them, and that resolving them requires a large numerical resolution. The latter is a significant hurdle in this context, as computing a single cyclic solution with a Newton-Krylov algorithm requires many DNS integrations. The resolution used in this study is (48, 48, 72), ensuring convergence for all parameters considered, but a few results were also reproduced at the (very computationally demanding) double resolution (96, 96, 144).

3. Chimera MRI dynamo cycles

3.1. Dynamical structure of the solutions

In order to identify cycles in moderate azimuthal to radial (L_y/L_x) aspect ratio shearing box simulations of the MRI dynamo problem, we explored the phase space of the system numerically by constructing turbulence lifetime maps using many different simulations initialised with different initial conditions. This technique, described in detail in R13, makes it possible to isolate islands of recurrent or chaotic dynamics in phase space. Once an initial condition leading to fairly recurrent dynamics was spotted, we used a Newton-Krylov solver described in H11 and R13 to refine the initial condition until a periodic solution is achieved. Using this technique, we managed to capture two pairs of nonlinear periodic solutions. The first one, labelled SN_{1m} , was found in a box of dimensions $(L_x, L_y, L_z) = (0.7, 6, 2)$ and has a period $T_{SN_{1m}} = 6 S^{-1} L_y/L_x = 51.4 S^{-1}$. The second one, labelled SN_{2m} , was found in a $(L_x, L_y, L_z) = (0.5, 2, 1)$ box, and has a slightly shorter period $T_{SN_{2m}} = 5 S^{-1} L_y/L_x = 20 S^{-1}$. Each pair of solutions is born out of a saddle node bifurcation and is therefore composed of a lower branch cycle and an upper branch cycle. These solutions are distinct from the different cy-

cles pairs studied by H11 and R13. The temporal evolutions of LB_{1m} (LB_{2m}), the lower branch of SN_{1m} (respectively SN_{2m}), are shown in Fig. 1.

The physical mechanisms and self-sustaining process underlying the dynamics of these two cycles are identical to those described by Rincon et al. (2007) and H11. The large scale axisymmetric component of the field $\bar{\mathbf{B}}_0$ renders non-axisymmetric velocity and magnetic perturbations unstable to the MRI in the Keplerian flow. For simplicity, we refer to these perturbations as “non-axisymmetric MRI-unstable shearing wave packets”¹. As they swing and their amplitude grows, these shearing wave packets transfer energy back to $\bar{\mathbf{B}}_0$ through nonlinear energy transfers in the form of a quadratic axisymmetric electromotive force (EMF) $\bar{\mathcal{E}}_0 = \bar{\mathbf{u}} \times \bar{\mathbf{B}}$, sustaining it against resistive effect (see Figs. 2 and 4 of H11 for detailed schematics and visualisations of the self-sustained dynamics).

The detailed dynamical complexity of SN_{1m} and SN_{2m} is significantly larger than that of cycles previously found in longer aspect ratio boxes, though:

- i) the successive reversals of $\bar{\mathbf{B}}_0$ are asymmetric in time.
- ii) each large-scale field reversal results from the accumulated nonlinear self-interactions of several successive MRI-unstable shearing wave packets, regularly separated in time by $L_y/L_x S^{-1}$ (the quantized time separation is a consequence of the symmetries of the shearing box model).
- iii) Besides, different shearing wave packets have a different energy content and polarization, and therefore they do not contribute equally to the large-scale field reversals.

These different properties are illustrated in Fig. 1. In the case of LB_{1m} , the first reversal (\bar{B}_0 , going from positive to negative) is caused by the combined action of three successive non-axisymmetric wave packets with different relative amplitudes (represented by dark blue, blue and cyan curves in the bottom panel). The second reversal also results from the combined action of three distinct wave packets (represented by green to yellow colors) with different relative amplitudes. The amplitudes of the second series of waves are also different from those of the first series, resulting in asymmetric $\bar{\mathbf{B}}_0$ reversals. For LB_{2m} , the asymmetry is even more pronounced: the first reversal only involves two wave packets, while the second involves three of them. Note that the period of LB_{1m} and LB_{2m} can be inferred directly from the product $L_y/L_x S^{-1}$ times the number of waves packets implicated in the cycle, because of the time quantization imposed by the symmetries of the shearing box. Finally, although

¹ We use this nomenclature because the MRI-unstable perturbations taking part in the dynamics documented in both H11 and in the present paper are essentially supported by non-axisymmetric $m = 1$ shearing Fourier modes. However, these perturbations are not reducible to a single Fourier mode in z , unlike in the uniform toroidal field case (Balbus & Hawley 1992), because the large-scale axisymmetric MRI-supporting “dynamo” field $\bar{\mathbf{B}}_0$ is non-uniform in z . More specifically, for the class of solutions considered here and in H11, the z -dependence of $m = 1$ velocity perturbations is decomposed in z as a sum over Fourier modes with odd n , and that of magnetic perturbations as a sum over even n (see Appendix of H11). Magnetic perturbations \mathbf{b} with $m = 1$ and even n are linearly coupled to velocity perturbations \mathbf{v} with $m = 1$ and odd n through inductive and Lorentz force terms $\bar{\mathbf{B}}_0 \cdot \nabla \mathbf{u}$ and $\bar{\mathbf{B}}_0 \cdot \nabla \mathbf{b}$ involving the non-uniform MRI-supporting axisymmetric azimuthal field $\bar{B}_{0y} \propto \cos(k_{z0} z)$ characterized by $(m = 0, n = 0)$. These couplings mediate the MRI. In all cases considered, we found that velocity perturbations are dominated by $(m = 1, n = 1)$, and magnetic perturbations by $(m = 1, n = 0)$ in the linear MRI growth phase.

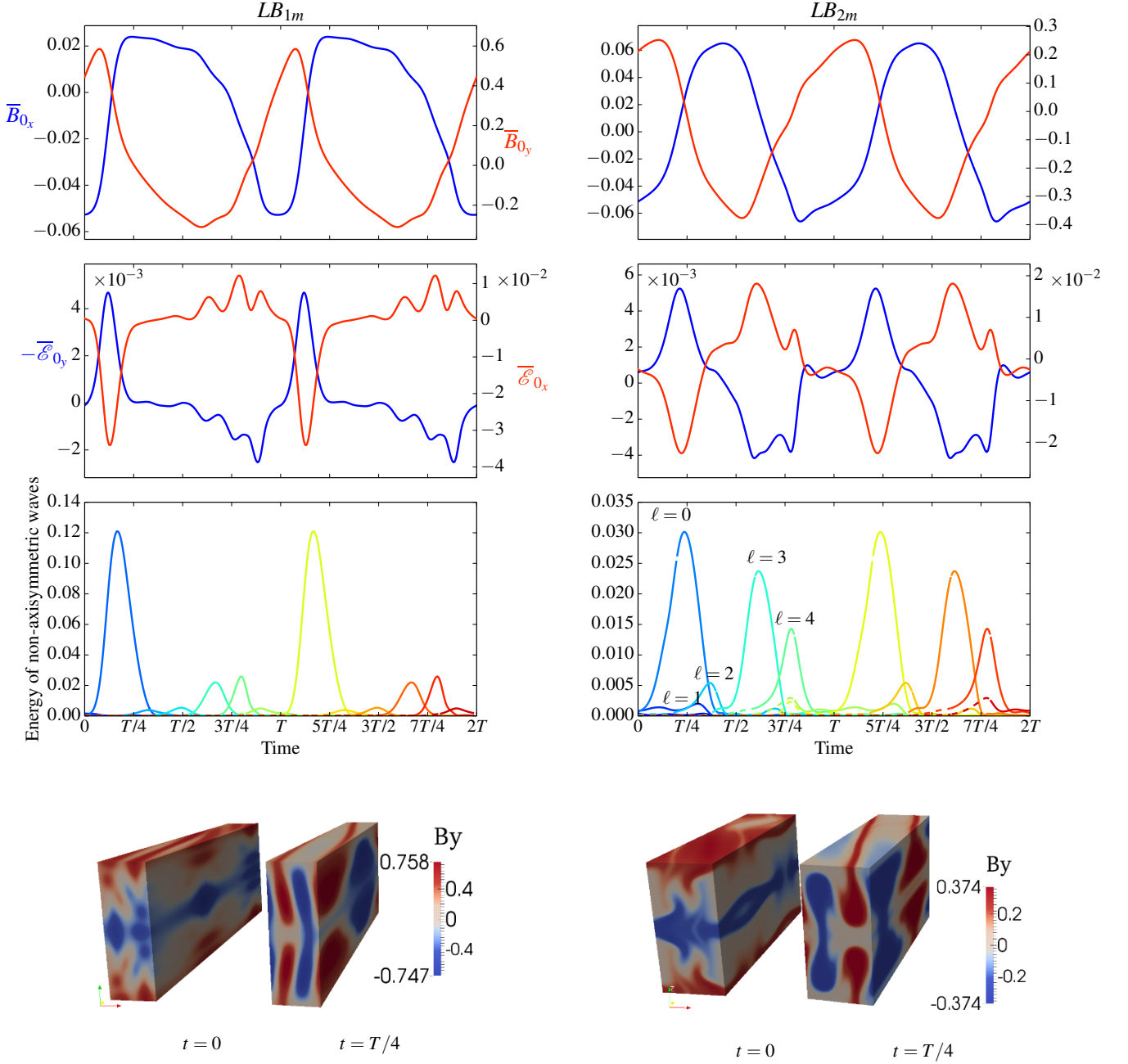


Fig. 1. Temporal evolution and dynamical decomposition of the lower branch solutions LB_{1m} (left) and LB_{2m} (right). LB_{1m} is shown for $Re = 100$, $Rm = 900$ and LB_{2m} for $Re = 908$, $Rm = 3033$. From top to bottom, axisymmetric field $\bar{\mathbf{B}}_0$, axisymmetric EMF (\mathcal{E}_{0x} , $-\mathcal{E}_{0y}$) and total energy (integrated over all k_z) of each shearing wave packet ($k_y = 2\pi/L_y$) as a function of time (2 cycle periods are represented). The rainbow colors and ℓ in the bottom plot represent successive shearing wave packets (see Sects. 2-4). The 3D visualizations show isosurfaces of B_y at $t = 0$ and $t = T_0/4$, where T_0 is the period of the corresponding cycle. Videos showing the total B_y and the poloidal velocity streamlines can be found at http://store.maths.cam.ac.uk/ASTRO/ar764/cycle_multish_Ly6.avi (for SN_{1m}) and http://store.maths.cam.ac.uk/ASTRO/ar764/cycle_multish_Ly2.avi (for SN_{2m}).

the dynamics of the MRI-supporting field $\bar{\mathbf{B}}_0$ is governed by the cumulative action of shearing wave packets, Fig. 1 shows that only a fraction of them are significantly amplified by the MRI and contribute to the EMF. We find that the evolution of these shearing wave packets, from the leading to the trailing phase, is influenced by nonlinear effects on top of their linear MRI amplification.

The complex multiscale behaviour of these “chimera” cycles is remarkable in the sense that it can still be understood in terms of simple building blocks of a nonlinear self-sustaining MRI dynamo process, but is also reminiscent of the fully turbulent butterfly dynamo states observed in generic MRI dynamo simulations (see for example the results of the incompressible simu-

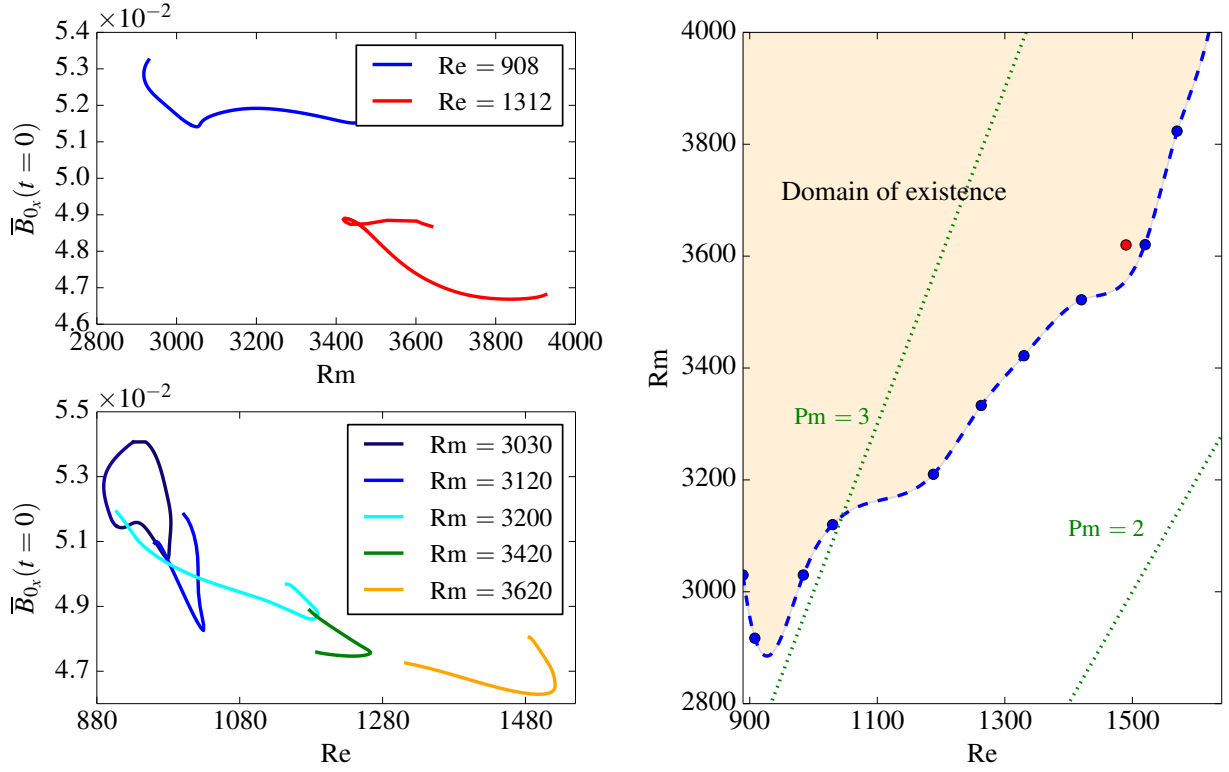


Fig. 2. Left, top panel: selected continuation curves in Rm of SN_{2m} at fixed Re ; bottom panel: selected continuation curves in Re at fixed Rm . Right: existence boundary of SN_{2m} in the (Re, Rm) plane (blue/dashed line) obtained by interpolating the different saddle node points $\text{Rm}_c(\text{Re})$ and $\text{Re}_c(\text{Rm})$ (blue bullets). The orange area shows the domain of existence of SN_{2m} in parameter space. The red bullet shows a saddle node bifurcation point computed at double resolution ($96 \times 96 \times 144$).

lations of Lesur & Ogilvie (2008a) for $(L_x, L_y, L_z) = (0.5, 2, 1)$. We will come back to this at length in Sect. 5.

The structure of these solutions finally suggests that self-sustained dynamo cycles with an arbitrarily long period can be constructed from successive MRI-unstable shearing wave packets (each new MRI-unstable shearing wave packet involved in the dynamics of the chimera cycles is generated consistently through a nonlinear physical process of scattering of its predecessor off the radially modulated axisymmetric magnetic field, see H11).

3.2. Cycle continuations and existence boundaries

In order to understand the physical origin of the dependence of the MRI dynamo on dissipative processes, R13 and R15 performed continuations in parameter space of different nonlinear cycles in elongated boxes, and found that their existence is systematically limited to Pm larger than unity. Because of the particular geometry used in these studies, it is natural to ask whether these conclusions can be extended to moderate aspect ratio boxes. We therefore performed a similar analysis for the more complex SN_{2m} pair in the $(L_x, L_y, L_z) = (0.5, 2, 1)$ box, as this cycle exhibits all the fundamental ingredients of the MRI dynamo process, and offers a good example of self-sustained semi-statistical MRI dynamo behaviour in moderate aspect ratio boxes. Although the full dynamics in this precise geometry almost certainly involves many other cycles, this is the only nonlinear periodic solution that we managed to compute and follow accurately in parameter space for this box.

Figure 2 (left) shows selected continuation curves for SN_{2m} . At fixed Re , these curves present a turning point at a critical

$\text{Rm}_c(\text{Re})$, confirming that SN_{2m} is born out of a saddle node bifurcation. At fixed Rm , we find that this pair of cycles exists only for a finite range of Re , whose upper bound increases as Rm increases. The domain of existence of SN_{2m} in parameter space, shown in Fig. 2 (right), is obtained by combining all the computed critical $\text{Rm}_c(\text{Re})$ and $\text{Re}_c(\text{Rm})$. The cycle existence is restricted to a region of Pm larger than unity for the range of Rm that could be probed². Hence, the results suggest that the conclusion of R13 and R15, that MRI dynamo cycles are only sustained in the region of Pm larger than unity, also hold in moderate aspect ratio boxes.

4. Energy budgets and turbulent dissipation

Studying the magnetic energy transfers between different modes involved in periodic nonlinear dynamics has previously proven useful to identify possible physical reasons for the seeming decay of the MRI dynamo at low Pm , and represents an important step towards a rigorous statistical description of this kind of dyto be subjectnamo. R15 showed that the subcritical "turbulent" magnetic diffusion associated with the development of a nonlinear cascade of MRI-unstable fluctuations to smaller scales at increasing Re has a destructive effect on both the large-scale MRI-supporting field and MRI-unstable fluctuations, and may explain the disappearance of dynamo cycles at moderate Rm and

² These continuations require a large computational effort. Each continuation curve in Fig. 2 (left) represents approximately 10 000 direct numerical simulations at resolution $48 \times 48 \times 72$. In addition, each branch can encounter many secondary bifurcations, which makes it hard to follow and complete them. We checked the numerical convergence of the results by doubling the resolution in a few cases.

low Pm in large aspect ratio boxes. Here, we aim to determine if the same conclusions hold for moderate aspect ratio dynamics by examining the energy budget of the saddle node pair SN_{2m} . This analysis is rather technical, and may be skipped by readers not interested in details. The conclusions are qualitatively the same as in R15, and are summarized in Sect. 6.

4.1. Energetics of the MRI supporting field $\bar{\mathbf{B}}_0$

The MRI dynamo intrinsically relies on the sustainment of a large-scale MRI-supporting magnetic field component against dissipative processes, which in shearing box simulations is dominated by the axisymmetric $\bar{\mathbf{B}}_0$. It is then of primary importance to analyse the energy budget of $\bar{\mathbf{B}}_0$ over a full cycle period $T_{SN_{2m}} = 5 S^{-1} L_y / L_x = 20 S^{-1}$,

$$\mathbf{\Omega}_0 + \mathbf{I}_0 + \mathbf{A}_0 + \mathbf{D}_0 = \mathbf{0}, \quad (5)$$

where

$$\mathbf{\Omega}_0 = -S \langle \bar{\mathbf{B}}_0 \bar{\mathbf{B}}_0 \rangle \mathbf{e}_y, \quad \mathbf{I}_0 = \langle \bar{\mathbf{B}}_0 \circ \bar{\mathbf{B}} \cdot \nabla \mathbf{u} \rangle, \quad (6)$$

$$\mathbf{D}_0 = -\left(k_{z0}^2 / \text{Rm}\right) \langle \bar{\mathbf{B}}_0 \circ \bar{\mathbf{B}}_0 \rangle, \quad \mathbf{A}_0 = -\langle \bar{\mathbf{B}}_0 \circ \overline{\mathbf{u} \cdot \nabla \mathbf{b}} \rangle \quad (7)$$

and $\langle \rangle$ denotes the volume and cycle period average and \circ the entrywise product $[(\mathbf{X} \circ \mathbf{Y})_i = X_i Y_i]$. $\mathbf{\Omega}_0$, \mathbf{I}_0 , \mathbf{A}_0 and \mathbf{D}_0 are the energetic contributions to $\bar{\mathbf{B}}_0$ respectively associated to the Ω -effect, nonlinear induction, nonlinear advection and ohmic dissipation. We also define $\mathbf{A}_{0;mi}$, the magnetic energy exchanged through nonlinear advection between $\bar{\mathbf{B}}_0$ and a given non-axisymmetric shearing wave packet, labelled m_i . Figure 3 shows the x and y projections of Eq. (5) for the lower branch of SN_{2m} as a function of Re , at fixed $\text{Rm} = 3030$ (the upper branch behaves similarly).

The MRI-supporting azimuthal field \bar{B}_{0y} loses most of its energy through the nonlinear advective transfer $A_{0y} < 0$, which acts as a weakly nonlinear “turbulent” diffusion. The laminar ohmic dissipation D_{0y} is negligible. The Ω effect is the only net source term for \bar{B}_{0y} , indicating that the sustainment of the radial \bar{B}_{0x} is critical for the dynamo process as a whole. Figure 3 (top) shows that \bar{B}_{0x} gains energy from both nonlinear induction I_{0x} and advection A_{0x} , and dissipates a large amount of this energy directly through ohmic diffusion. The part of A_{0x} associated with the nonlinear correlations of the dominant MRI-unstable ($m = 1, n = 1$) velocity perturbation and ($m = 1, n = 0$) magnetic perturbation (denoted by $A_{0;a1x} > 0$ in the figure, anticipating the notations introduced in Sect. 4.3.1 below) is positive, and much larger than the total A_{0x} . This implies that some energy is also transferred nonlinearly from \bar{B}_{0x} to other smaller-scale modes, which can be interpreted again as a turbulent diffusion acting on \bar{B}_{0x} .

This budget is reminiscent of the results of R15 for large aspect ratio cycles. The most notable difference is that I_{0x} is not small here, and is of the order A_{0x} . While this term may also be important for the sustainment of the dynamo and for the Pm problem (as Re increases, I_{0x} decreases while A_{0x} increases), in the following we focus on the role of A_{0x} in relation to the results of R15.

4.2. Energetics of shearing wave packets

In the previous analysis, the key quantity A_{0x} included both the (positive) energy exchanged nonlinearly between \bar{B}_{0x} and MRI-unstable perturbations and the (negative) energy exchanged between \bar{B}_{0x} and other smaller-scale perturbations, integrated over

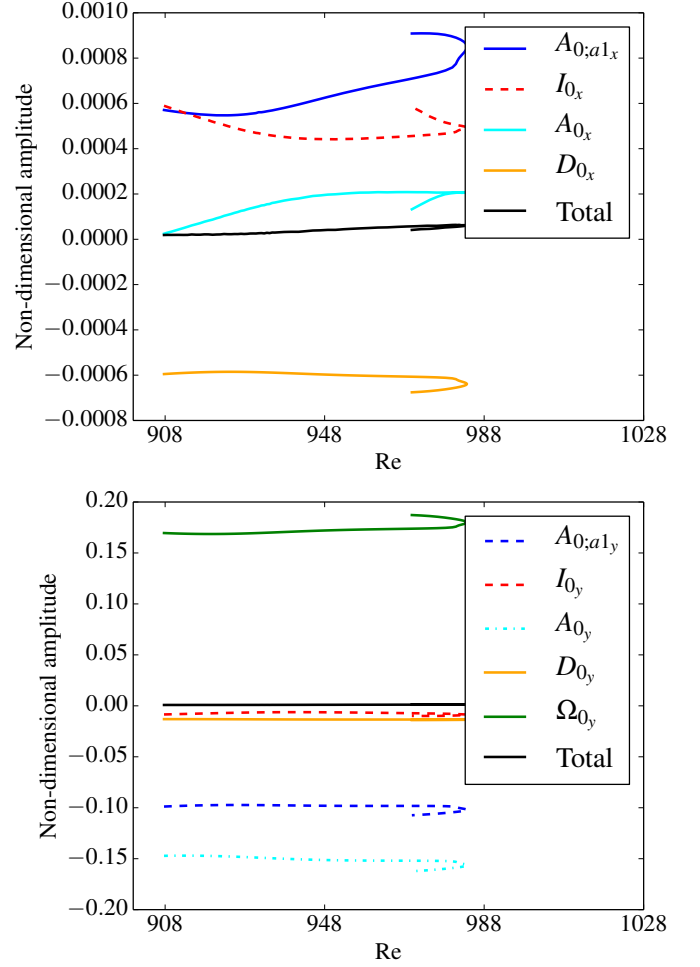


Fig. 3. x - (top) and y - (bottom) projections of the energy budget (5) of the axisymmetric field component $\bar{\mathbf{B}}_0$ of LB_{2m} as a function of Re ($\text{Rm} = 3030$).

a full period of SN_{2m} . To understand the details of these energy transfers in moderate aspect ratio boxes, we now investigate the magnetic energy budget of individual non-axisymmetric wave packets ($m \neq 0$). Wave packets with different lagrangian radial wavenumbers ℓ differing by $\Delta\ell = 1$ swing in the box one after the other at regularly spaced time intervals, and we label each successive packet by its superscript ℓ . For SN_{2m} , ℓ varies from 0 to 4 (the evolution of total energy of each of these waves is shown in Fig. 1). $m = 1$ wave packets, which dominate the dynamics here, have a typical swinging time $S^{-1} L_y / L_x$. The magnetic energy budget for a given (m, n) , summed over all successive ℓ waves, reads

$$\mathbf{\Omega}_{(m,n)} + \mathbf{I}_{(m,n)} + \mathbf{A}_{(m,n)} + \mathbf{D}_{(m,n)} \simeq \sum_{\ell} \left\langle \mathbf{b}_{(m,n)}^{\ell} \circ \frac{\partial}{\partial t} \mathbf{b}_{(m,n)}^{\ell} \right\rangle \simeq \mathbf{0}. \quad (8)$$

Here, $\mathbf{\Omega}_{(m,n)}$, $\mathbf{I}_{(m,n)}$, $\mathbf{A}_{(m,n)}$ and $\mathbf{D}_{(m,n)}$ are energetic contributions associated to the Ω -effect, nonlinear induction, nonlinear advection and ohmic dissipation,

$$\mathbf{\Omega}_{(m,n)} = - \sum_{\ell} S \langle \bar{\mathbf{b}}_{(m,n)x}^{\ell} \bar{\mathbf{b}}_{(m,n)y}^{\ell} \rangle \mathbf{e}_y, \quad (9)$$

$$\mathbf{I}_{(m,n)} = \sum_{\ell} \langle \mathbf{b}_{(m,n)}^{\ell} \circ (\mathbf{B} \cdot \nabla \mathbf{u})_{(m,n)}^{\ell} \rangle, \quad (10)$$

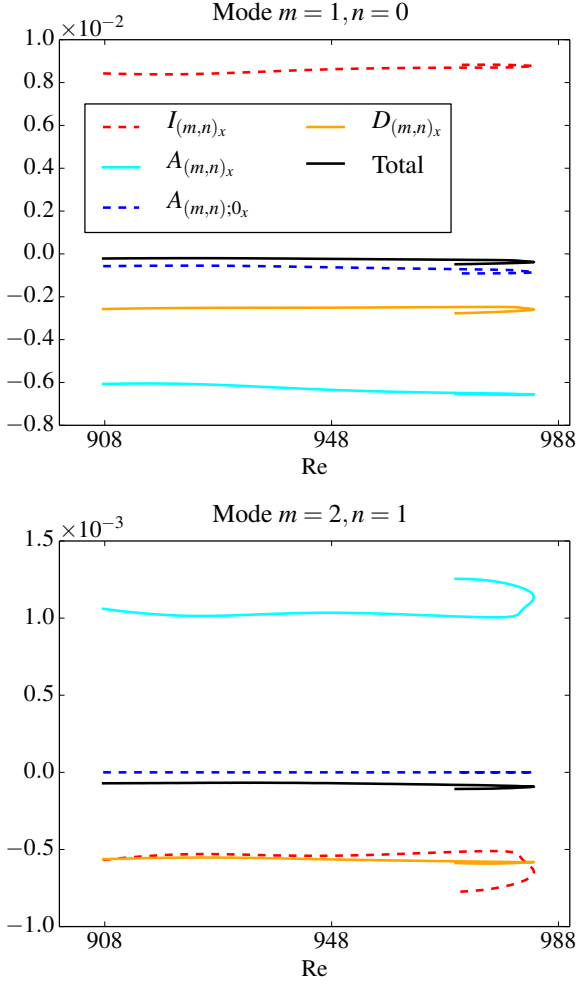


Fig. 4. x -projection of the cumulated magnetic energy budgets (8) of non-axisymmetric perturbations as a function of Re , for the lower branch LB_{2m} at $Rm = 3030$. Top: active MRI-unstable perturbation a_1 (magnetic perturbation $m = 1, n = 0$). Bottom: slaved MRI-stable magnetic perturbation ($m = 2, n = 1$). The sum of all source and dissipative terms remains close to 0.

$$\mathbf{D}_{(m,n)} = - \sum_{\ell} \eta k^2 \langle \mathbf{b}_{(m,n)}^{\ell} \circ \mathbf{b}_{(m,n)}^{\ell} \rangle, \quad (11)$$

$$\mathbf{A}_{(m,n)} = \sum_{\ell} \langle \mathbf{b}_{(m,n)}^{\ell} \circ (\mathbf{u} \cdot \nabla \mathbf{B})_{(m,n)}^{\ell} \rangle. \quad (12)$$

The advective term $\mathbf{A}_{(m,n)}$ basically represents the magnetic energy exchanged between (m, n) and all the other modes. The budget is only approximatively zero because each ℓ waves carries a tiny amount of energy in the strongly leading and trailing phases, and has (very weak) nonlinearly couplings to its predecessors and successors (see H11). These couplings can be neglected in the context of this particular energetic analysis. We now analyse the energy budget of two illustrative “active” and “slaved” non-axisymmetric perturbations taking part in the dynamics of LB_{2m} .

4.2.1. Active perturbations

We first consider magnetic perturbations with $(m = 1, n = 0)$. As explained in the footnote in Sect. 3, these perturbations, in conjunction with $(m = 1, n = 1)$ velocity perturbations, dominate

the non-axisymmetric MRI-unstable dynamics in the system under consideration. They are subject to energy injection through induction and, through their non-linear EMF coupling $\overline{\mathbf{u}} \times \overline{\mathbf{b}}$ to $(m = 1, n = 1)$ velocity perturbations, act as the main energy provider of $\overline{\mathbf{B}}_0$ through nonlinear transfers. We therefore label this set of non-axisymmetric perturbations as a_1 for “active”.

The energetics of the radial component of these magnetic perturbations is illustrated in Figure 4 (top), which shows the radial projection of Eq. (8) for $(m = 1, n = 0)$ a function of Re . As expected of an MRI-unstable situation, energy is gained through the induction term ($I_{a_1,x} > 0$), and redistributed through nonlinear advective transfers ($A_{a_1,x} < 0$) to both $\overline{\mathbf{B}}_0$ and smaller-scale modes. The azimuthal component (not shown) extracts energy through the Ω -effect. Other $m = 1$ magnetic modes with $n = 2, 4$ behave in the same way.

A short digression is in order. Here and before, we have taken a Eulerian viewpoint, which is easier to analyse numerically but not necessarily very transparent physically. The previous results simply mean that the large-scale “lagrangian” magnetic field, described in a good first approximation by the sum of $\overline{\mathbf{B}}_0$ and shearing non-axisymmetric $m = 1$ waves (and multiple n) at the Re and Rm considered, is basically sustained by MRI induction ($I_{a_1,x}$). The nonlinear advective transfers between $\overline{\mathbf{B}}_0$ and a_1 redistribute energy between these two Eulerian modes but conserve their total energy (see H11, Fig. 4 for a lagrangian picture of MRI dynamo reversals).

4.2.2. Slaved perturbations

The previous analysis explains how the large-scale field can be sustained through a dynamo process involving non-axisymmetric MRI-unstable wave packets. However, not all perturbations that take part in the nonlinear dynamics of LB_{2m} are excited by the MRI nor feed back energy into the large-scale dynamo field. As can be seen in Fig. 4 (bottom), magnetic perturbations such as $m = 2, n = 1$ have $I_{(m,n),x} < 0$ and $A_{(m,n),x} > 0$ (a similar budget is obtained for $m \geq 2$ and $n \geq 1$). Such “slaved” perturbations represent smaller-scale structures which are not themselves amplified by the MRI. They only gain energy through nonlinear transfers from larger-scale MRI-amplified active perturbations, and dissipate it through laminar dissipation. In other words, they act as a “turbulent” diffusion for the large scale field and are therefore destructive for the dynamo. We will use this separation between “active” and “slaved” perturbations in the next paragraph to quantify this diffusion in a global way as function of Re and Rm .

4.3. Characterization of turbulent magnetic dissipation

4.3.1. Formalism

We now use the previous concept of active and slaved perturbations to characterize turbulent magnetic diffusion more quantitatively, and to study its impact on the dynamo at large Re (low Pm). A Fourier mode will be considered as active if

$$I_{(m,n),x} > 0 \quad \text{and} \quad A_{(m,n),x} < 0. \quad (13)$$

These modes will be labelled $a_i = 1, \dots, N_a$. On the contrary, a magnetic mode will be considered as slaved if $I_{(m,n),x} < 0$ or $A_{(m,n),x} > 0$. Slaved modes are stabilized with respect to the MRI by a stronger diffusion and magnetic tension, and will be labelled $s_i = 1, \dots, N_s$. “Small-scale” axisymmetric modes ($m = 0, n > 1$)

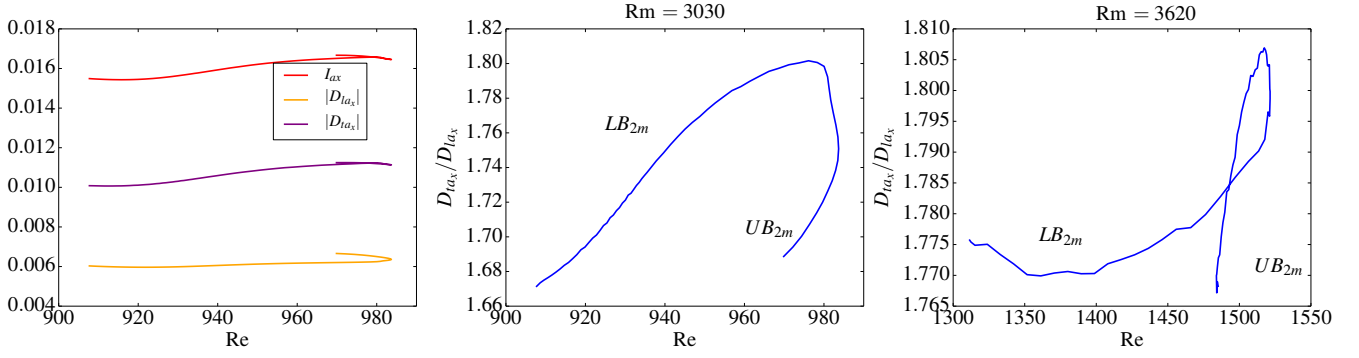


Fig. 5. Left panel: the different terms I_{ax} , D_{la_x} and D_{ta_x} in the net magnetic energy budget (20) for LB_{2m} as a function of Re , at fixed $Rm = 3030$. Middle and right panels: ratio D_{ta_x}/D_{la_x} for the lower and upper branches of SN_{2m} as a function of Re , for $Rm = 3030$ and $Rm = 3620$ respectively (the roughness of the rightmost plot is due to the limited time-sampling of simulation outputs used in the postprocessing analysing stages, not to the numerical resolution of the simulations).

will also be considered as slaved because they do not contribute directly to the sustainment of $\bar{\mathbf{B}}_0$.

We can then think of turbulent diffusion as the cumulated nonlinear effect of all slaved modes on all the active ones and on $\bar{\mathbf{B}}_0$. The same idea was used in R15 to characterize turbulent diffusion for large aspect ratio cycles. The only difference here is that the physical structure of non-axisymmetric active MRI perturbations taking part in the dynamics of chimera cycles is more complex (it involves a larger number of m and n Fourier modes), and that these cycles involve a succession of such non-axisymmetric structures (different ℓ , see Fig. 1).

We define the amount of energy exchanged during a cycle period between a mode (m, n) and a mode (m', n') :

$$\mathbf{A}_{(m,n);(m',n')} = -\langle \mathbf{b}_{(m,n)} \circ (\mathbf{u}_{(m-m',n-n')} \cdot \nabla \mathbf{b}_{(m',n')}) \rangle \quad (14)$$

with

$$\mathbf{A}_{(m,n);(m',n')} = -\mathbf{A}_{(m',n');(m,n)}. \quad (15)$$

We then have the following relation, using the active/slaved shorthand notation:

$$\mathbf{A}_0 = \sum_{j=1}^{N_a} \mathbf{A}_{0;a_j} + \sum_{j=1}^{N_s} \mathbf{A}_{0;s_j}, \quad (16)$$

$$\mathbf{A}_{a_i} = \mathbf{A}_{a_i;0} + \sum_{j \neq i} \mathbf{A}_{a_i;a_j} + \sum_{j=1}^{N_s} \mathbf{A}_{a_i;s_j}, \quad (17)$$

which simply expresses that any active mode exchanges energy with the background field $\bar{\mathbf{B}}_0$, the other active modes and the slaved modes. We define the turbulent dissipation \mathbf{D}_{ta} as the total magnetic energy nonlinearly transferred from the system $\{\bar{\mathbf{B}}_0 + \text{active modes}\}$ to the slaved modes:

$$\mathbf{D}_{ta} = \sum_{j=1}^{N_s} \mathbf{A}_{0;s_j} + \sum_{i=1}^{N_a} \sum_{j=1}^{N_s} \mathbf{A}_{a_i;s_j}. \quad (18)$$

We now focus on the x -component of Eq. (18), as it is the most critical for the sustainment of the dynamo (the y -component of the magnetic field always benefits from the Ω -effect). Summing Eq. (17) over all the active modes, using Eq. (16) and the symmetry condition (15), we obtain

$$D_{ta_x} = A_{0_x} + \sum_{j=1}^{N_a} A_{a_{j_x}}. \quad (19)$$

Finally, summing the energy budget (8) over all the active modes, and adding the contribution of the axisymmetric field $\bar{\mathbf{B}}_0$ to the result, we obtain the effective magnetic energy budget of the active radial field component,

$$\underbrace{\left(I_{0_x} + \sum_{i=1}^{N_a} I_{a_{i_x}} \right)}_{I_{ax}} + \underbrace{\left(D_{0_x} + \sum_{i=1}^{N_a} D_{a_{i_x}} \right)}_{D_{la_x}} + D_{ta_x} \simeq 0. \quad (20)$$

The first curly brace term I_{ax} is the net magnetic energy injected in the system $\{\bar{\mathbf{B}}_0 + \text{active modes}\}$ over a cycle period. The second curly brace term D_{la_x} , is the magnetic energy directly lost by $\bar{\mathbf{B}}_0$ and active modes through “laminar” ohmic dissipation. Finally, by construction and as desired, D_{ta_x} stands for the energy lost by these modes through nonlinear energy transfers to smaller scales. This equation indicates that the magnetic energy injected via the MRI into the active dynamo field balances the sum of laminar and turbulent magnetic dissipations (for a periodic solution).

4.3.2. Turbulent magnetic dissipation for SN_{2m}

Having been through great pains to formalise the analysis of the magnetic energy budgets of the MRI dynamo in the shearing box, we can now apply it to the SN_{2m} chimera cycles. Figure 5 (left) shows the induction term I_{ax} and the two dissipative terms D_{la_x} and D_{ta_x} for this pair of cycles as a function of Re , at fixed $Rm = 3030$. It appears that the turbulent dissipation D_{ta_x} for both lower and upper branches increases significantly more rapidly than the laminar dissipation D_{la_x} as Re is increased. As shown in Fig. 5 (middle and right panels), this ratio D_{ta_x}/D_{la_x} increases by 7% from $Re = 910$ to $Re = 980$. The same result holds at the larger $Rm = 3620$ at which the cycle is sustained for a wider range of Re . These results therefore suggest that the disappearance of cycles at large Re is caused by the relative enhancement of turbulent magnetic dissipation associated with the development of smaller-scale velocity fluctuations. At larger Re , this additional dissipation can only be compensated if we can make induction larger relative to laminar dissipation, i.e. by going to larger Rm . This seems to explain well the typical existence boundary of MRI dynamo cycles in the (Re, Rm) plane.

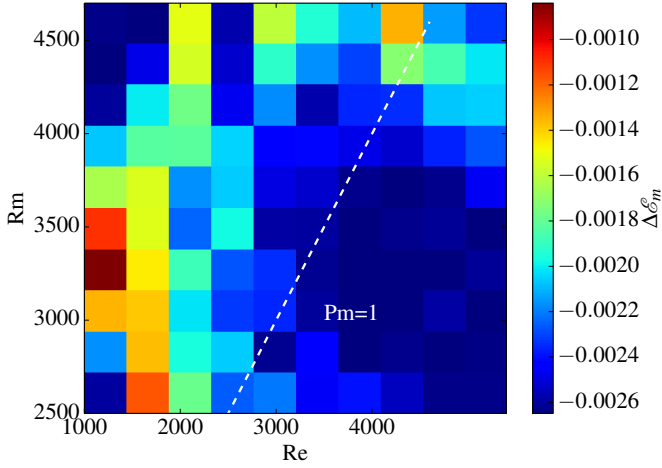


Fig. 6. Magnetic energy change $\Delta\mathcal{E}_m$ of the axisymmetric radial magnetic field component \bar{B}_{0x} between $t = 0$ and $T_{SN_{2m}} = 5S^{-1}L_y/L_x$ for simulations at different Re and Rm initialized with the same initial condition consisting of the MHD state $LB_{2m}(t = 0)$ at Re = 908 and Rm = 3030.

4.3.3. Illustration of turbulent magnetic dissipation in aperiodic test simulations

To investigate whether the conclusions of the previous analysis pertain to more general circumstances and can explain the seeming disappearance of the MRI dynamo as a whole at low Pm, we finally considered slightly more generic aperiodic test simulations in the phase-space vicinity of SN_{2m} . We performed a series of simulations at different Re and Rm initialized with the same initial condition, consisting of the initial state of the LB_{2m} cycle computed at Re = 908 and Rm = 3030. Except for these precise values of Re and Rm, the time evolution from this initial condition is not periodic and can result in either a gain or loss of magnetic energy after an integration of the equations over a period of the original cycle $T_{SN_{2m}} = 5S^{-1}L_y/L_x$. We then computed the magnetic energy change $\Delta\mathcal{E}_m$ in the \bar{B}_{0x} component after this time, as a function of Re and Rm. Figure 6 shows that $\Delta\mathcal{E}_m$ is always negative for Re > 908, and that the energy loss increases with Re at fixed Rm (or equivalently lower Pm). Moreover, the nonlinear term A_{0x} responsible for the sustainment of \bar{B}_{0x} decreases with Re. Although the latter result does not rigorously quantify the turbulent dissipation, it indicates that some magnetic energy injected into MRI-unstable waves is transferred to small scales rather than into \bar{B}_{0x} at large Re, resulting in the decay of the MRI-supporting field and therefore of the dynamics as a whole.

Figure 7 provides a direct physical illustration of the effects of turbulent magnetic diffusion at large Re. The visualizations show the vertical velocity field and total radial magnetic field B_x in a poloidal (x, z) plane around the time of reversal of \bar{B}_0 . At Re = 5000, vertical velocity field perturbations clearly have more small-scale structure than at Re = 908, and the non-axisymmetric counter-rotating flow vortices driving the reversal of the large-scale field (see H11) are much less regular. The magnetic field inherits some of this small-scale structure through “turbulent” advection. The magnetic gradients (electric currents) are clearly larger at Re = 5000 than at Re = 908, leading to enhanced magnetic dissipation.

5. The missing link to turbulent accretion disk dynamo models ?

As shown in Sect. 3, chimera dynamo cycles can be understood in terms of simple physical building blocks of a nonlinear self-sustaining MRI dynamo process, but are also reminiscent of the statistical butterfly states observed in many simulations. The structure of chimeras suggests that cycles made of a large number of MRI-unstable shearing wave packets (dynamo “quanta”) can be constructed in shearing boxes of different aspect ratio (at least for $Pm > 1$). Although they do not accommodate all the physical elements entering the accretion disk dynamo problem (such as magnetic buoyancy), the dynamical behaviour of these structures therefore raises the prospect that a statistical theoretical MRI dynamo model can be rigorously derived from first principle physics. The aim of this section is to highlight some important dynamical features of the solutions at hand, some but not all of which are already taken into account in existing theoretical models (Lesur & Ogilvie 2008b,a; Gressel 2010; Gressel & Pessah 2015; Squire & Bhattacharjee 2015), in order to provide constructive guidance for future work on statistical theory.

5.1. Statistical linearity vs dynamical nonlinearity

To introduce the matters, we reproduce in Fig. 8 (top) the instantaneous relationship between the large-scale axisymmetric nonlinear EMF $\bar{\mathcal{E}}_0$ and \bar{B}_0 for the lower branch cycles LB_1 and LB_2 computed by H11 and R13 in azimuthally elongated shearing boxes. As noted in H11, the standard mean-field theory ansatz of a linear relationship (Steenbeck et al. 1966; Moffatt 1977; Brandenburg & Subramanian 2005, see Gressel 2010; Blackman 2012; Gressel & Pessah 2015 for applications to the accretion disk dynamo context) doesn’t fit these solutions of the full MHD equations (a similar mismatch has been reported for a magnetic-buoyancy driven dynamo, see Cline et al. (2003)). A possible explanation for this discrepancy is that such solutions, despite being nonlinear, are not turbulent or statistical in essence, and that the linear mean-field relationship only holds statistically. The question nevertheless arises as to whether and how one can rigorously relate the fundamental linear and nonlinear physical processes illustrated by these three-dimensional solutions to a seemingly more abstract statistical two-dimensional effective description. Of particular concern with the mean-field description in the context of instability-driven dynamos (such as the MRI dynamo) is the lack of explicit connection between mean-field effects and fundamental dynamical processes (such as the MRI) in the absence of which there can be no dynamo-generating turbulence at all in the first place in the corresponding systems.

This possible limitation of classical mean-field theory has motivated the development of alternative quasi-linear models of the turbulent MRI dynamo describing the cumulated effects of a statistical assembly of shearing waves whose individual physical linear evolution can be computed consistently either analytically or numerically (Lesur & Ogilvie 2008a,b; Squire & Bhattacharjee 2015). The structure of our chimera dynamo cycles qualitatively vindicates this approach (albeit with a few caveats to be discussed below). Another encouraging sign that it may be possible to close in on a fully self-consistent statistical theory is illustrated by Figure 8 (bottom), which now shows the instantaneous relationship between the large-scale axisymmetric nonlinear $\bar{\mathcal{E}}_0$ and \bar{B}_0 for the lower branch chimera cycles LB_{1m} and LB_{2m} . While the detailed relationship remains nonlinear, a clear average linear trend emerges in comparison to the LB_1 and LB_2

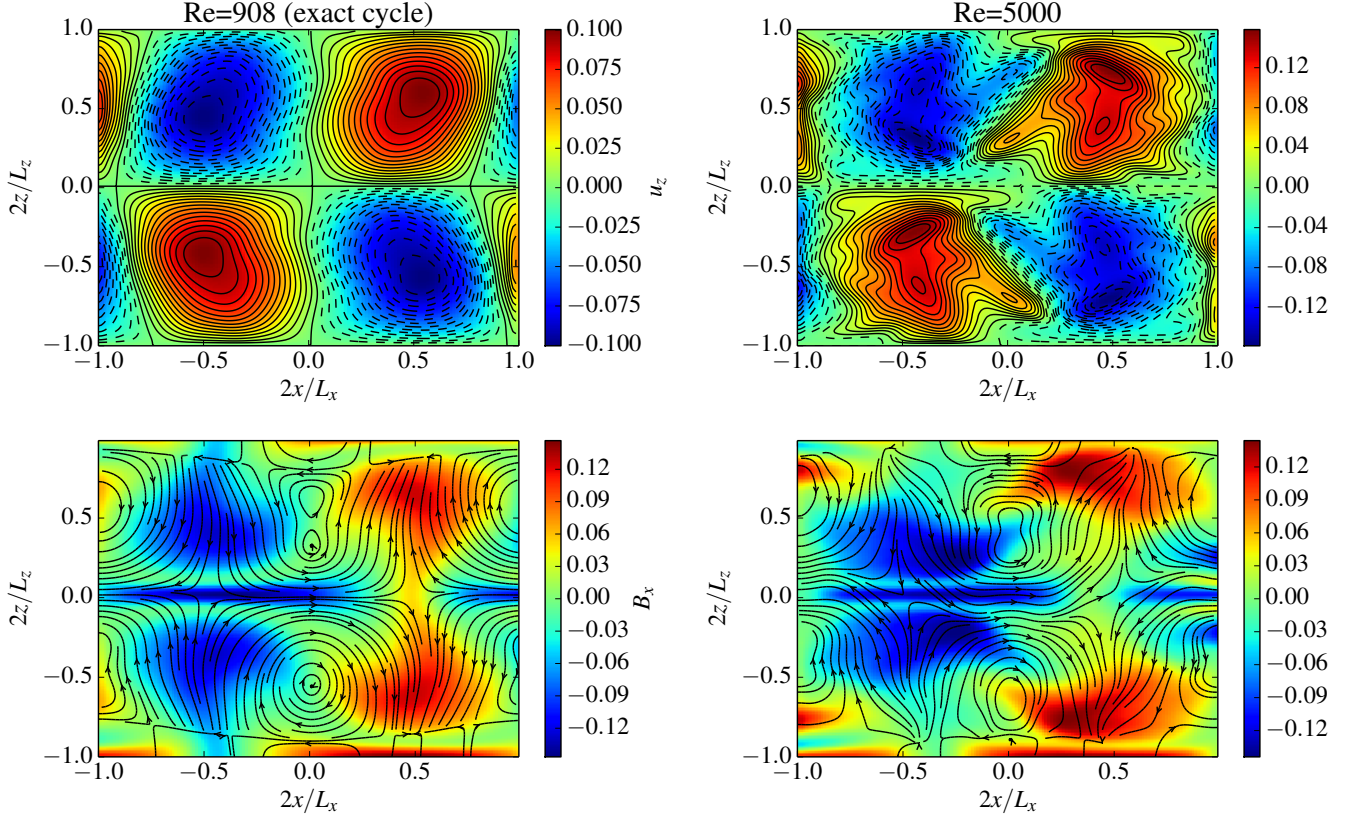


Fig. 7. Color snapshots of the vertical velocity field u_z (top) and radial magnetic field B_x (bottom) in the poloidal plane (x, z) . Left panel: LB_{2m} at $Re = 908$. Right panel: MHD state integrated from the same initial condition, but at $Re = 5000$. $Rm = 3030$ in both cases. The snapshots are taken at the time $t = 5 S^{-1}$ around which the first $\bar{\mathbf{B}}_0$ reversal of LB_{2m} occurs. The dashed black lines are iso-contours of u_z , the full black lines with arrows are poloidal velocity streamlines.

cases. This result supports the common intuition that complex three-dimensional nonlinear multiscale dynamics tend to generate statistically simple effective large-scale dynamical states in the turbulent limit.

5.2. Roles of active and passive perturbations

The most direct explanation for a statistical correlation between the large-scale EMF and large-scale magnetic field in the MRI dynamo problem can be found in the quasi-linear theory of Lesur & Ogilvie (2008a), which predicts a linear dependence between the MRI-supporting field and the nonlinear EMF generated by MRI-amplified shearing waves packets. This is notably expected if the MRI-supporting toroidal field \bar{B}_{0y} and azimuthal wavenumbers of the shearing waves are such that the MRI is on its weak-field branch, so that the MRI growth rate is proportional to \bar{B}_{0y} . In a simulation, one would therefore expect that successive shearing waves “see” a slowly time-evolving large-scale field and that their relative growth (and ensuing nonlinear EMF feedback) is modulated according to the amplitude of the MRI-supporting field at the time of their amplification, resulting in the linear trend discussed above. This correlation is not observed for individual ℓ shearing wave packets of our chimera cycles (individual wave amplitudes do not seem to be directly linked to either the sign or amplitude of $\bar{\mathbf{B}}_0$) but certainly holds in an average sense (otherwise we would not be able to observe regular field reversals).

Another possible (but as yet unscrutinized) explanation to explain the average linear trend described above is that each new MRI-unstable shearing wave packet involved in the chimera dynamics is nonlinearly seeded through a physical process of scattering of its predecessor off the radially modulated large-scale axisymmetric magnetic field (see H11 for a detailed discussion of this effect), resulting in some statistical correlation between the cumulated nonlinear EMF associated with swinging shearing waves and the large-scale field. The early polarization of shearing wave seeds in their strongly leading phase, though, may not be particularly optimal in terms of MRI amplification which, considering their limited lifetime, may explain why they produce seemingly wildly different EMFs (we recall that each shearing wave only has a finite time to grow before it is strongly damped – for LB_{2m} with $L_y/L_x = 4$ aspect ratio, their “active” lifetime is of the order of few Ω^{-1} at most). Note that existing quasi-linear statistical models randomly drawing shearing wave seeds are currently blind to such scattering effects. Whether this is a limitation remains to be assessed.

Implicit to the discussion above is that the sustainment of the dynamo results from the cumulated effect of MRI-active perturbations as defined in Sect. 4. While it contrasts with the classical view of mean-field effects being related to small-scale, “inertial-range” turbulence, this hypothesis is definitely supported by our numerical simulations and magnetic energy bud-

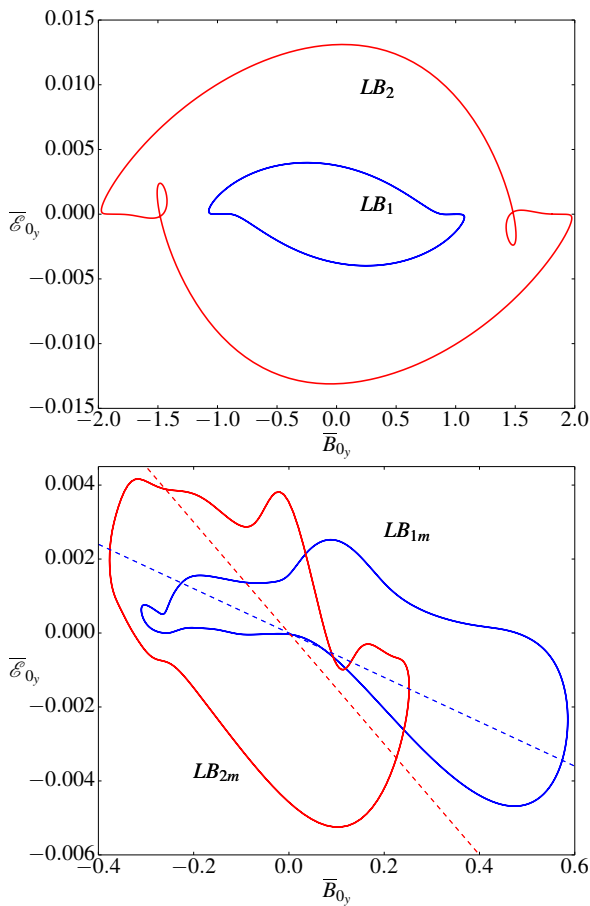


Fig. 8. Phase portraits of periodic dynamo solutions in the \mathcal{E}_{0y} vs \bar{B}_{0y} plane (large-scale axisymmetric EMF vs large-scale axisymmetric azimuthal field). Top: lower branches of the two cycles LB_1 and LB_2 computed in a large aspect ratio box $L_y/L_x = 28.57$ (see H11 and R13). Bottom: new chimera lower branches LB_{1m} and LB_{2m} computed in moderate aspect ratio boxes (0.7, 6, 2) and (0.5, 2, 1). The dashed lines indicate the linear trend between \mathcal{E}_{0y} and \bar{B}_{0y} .

get analysis³, as well as by other recent numerical results (Bhat et al. 2016). However, another result of the analysis conducted in Sect. 4 is that smaller-scale slaved waves excited mostly through nonlinear interactions (which are also not self-consistently computed in quasi-linear models) are also important in this problem, and notably play an important role in the magnetic Prandtl number dependence of the dynamo through the effect of turbulent magnetic dissipation.

Hence, it is tempting at this stage to sketch a refined physical picture of the full turbulent MRI dynamo process (and more generally of turbulent instability-driven dynamos) in which the EMF associated with non-universal, fairly large-scale active modes feeling the effect of the linear physics constitutes the main engine of the dynamo, while faster, smaller-scale “inertial-range” slaved modes can either impede it (as in our chimera cycles) or reinforce it further (depending on the problem). If this physical picture holds, then the decomposition presented in Sect. 4.3.1 may prove extremely useful to construct more trans-

parent, physically-grounded statistical mean-field dynamo models out of the existing ones.

6. Conclusions

Motivated by the quest for a physically-grounded description of the nonlinear process of turbulent dynamo action and angular momentum transport in astrophysical accretion disks, we have computed several new periodic, three-dimensional, fully nonlinear incompressible magnetorotational dynamo solutions in moderate aspect ratio shearing boxes. The dynamical complexity of these “chimera” solutions is significantly larger than that of solutions identified earlier by H11, R13 and R15, and is reminiscent of the seemingly complex statistical magnetic organization observed in many fully turbulent simulations of the problem. Yet, we have shown that their sustainment can be understood in terms of the same few linear and nonlinear dynamical processes underlying simpler cycles. These solutions, like their simpler counterparts (R15), are also not sustained for magnetic Prandtl numbers smaller than a few.

In order to understand the dynamics in a physically transparent way, we have introduced a decomposition into active and slaved modes. The former include a large-scale axisymmetric MRI-supporting field component, and non-axisymmetric MRI-unstable energy-injecting perturbations. The latter consist of perturbations passively excited through nonlinear interactions that drain energy from larger scales. Using this decomposition, we have been able to understand how the magnetic energy of the system can be sustained via the MRI, and to confirm the results of R15 regarding the role of turbulent magnetic dissipation in the seeming disappearance of the MRI dynamo at low Pm. With this basic effect identified and confirmed, it may now be possible to better understand how it affects the dynamo and turbulent angular momentum transport in different geometric and physical configurations (Shi et al. 2016; Walker et al. 2016).

The results presented in this paper are obviously not in the astrophysically asymptotic regimes and do not accommodate all the relevant physics in this context, such as magnetic buoyancy and stratification effects. However, we have shown that our physically transparent, fully three-dimensional, nonlinear magnetorotational dynamo chimeras share some interesting properties with existing effective two-dimensional statistical models of accretion disk dynamo cycles and as such seem to offer an interesting path in parameter space towards statistical asymptotic regimes. This raises the prospects that improved effective statistical models of the MRI dynamo and other instability-driven dynamos (Spruit 2002; Cline et al. 2003; Miesch et al. 2007; Rincon et al. 2008) can be derived from physical first principles, and may in the near future provide trustable insights into magnetic field generation and turbulent transport processes in a variety of stellar and circumstellar environments.

Acknowledgements. We thank Richard Kerswell, Sébastien Fromang, Jonathan Squire and Oliver Gressel for several useful discussions. This research was supported by the University Paul Sabatier of Toulouse under an AO3 grant, by the Midi-Pyrénées region, by the French National Program for Stellar Physics (PNPS), by the Leverhulme Trust Network for Magnetized Plasma Turbulence and by the National Science Foundation under Grant No. PHY05-51164. Numerical calculations were carried out on the CALMIP platform (CICT, University of Toulouse), whose assistance is gratefully acknowledged.

References

- Balbus, S. A. & Hawley, J. F. 1991, *ApJ*, 376, 214
- Balbus, S. A. & Hawley, J. F. 1992, *ApJ*, 400, 610

³ To complicate the matters further, note that such linear growth effects are in principle captured by test field method calculations (Gressel 2010; Gressel & Pessah 2015), whose original motivations are rooted in the classical mean field theory.

- Balbus, S. A. & Henri, P. 2008, ApJ, 674, 408
- Bhat, P., Ebrahimi, F., & Blackman, E. G. 2016, submitted [arXiv:1605.02433]
- Blackman, E. G. 2012, Phys. Scr., 86, 058202
- Brandenburg, A., Nordlund, A., Stein, R. F., & Torkelsson, U. 1995, ApJ, 446, 741
- Brandenburg, A. & Subramanian, K. 2005, Phys. Rep., 417, 1
- Chandrasekhar, S. 1960, Proc. Natl. Acad. Sci., 46, 253
- Cline, K. S., Brummell, N. H., & Cattaneo, F. 2003, ApJ, 599, 1449
- Davis, S. W., Stone, J. M., & Pessah, M. E. 2010, ApJ, 713, 52
- Fromang, S., Papaloizou, J., Lesur, G., & Heinemann, T. 2007, A&A, 476, 1123
- Goldreich, P. & Lynden-Bell, D. 1965, MNRAS, 130, 125
- Gressel, O. 2010, MNRAS, 405, 41
- Gressel, O. & Pessah, M. E. 2015, ApJ, 810, 59
- Hawley, J. F., Gammie, C. F., & Balbus, S. A. 1995, ApJ, 440, 742
- Hawley, J. F., Gammie, C. F., & Balbus, S. A. 1996, ApJ, 464, 690
- Herault, J., Rincon, F., Cossu, C., et al. 2011, Phys. Rev. E, 84, 036321
- Lesur, G. & Longaretti, P.-Y. 2007, MNRAS, 378, 1471
- Lesur, G. & Ogilvie, G. I. 2008a, MNRAS, 391, 1437
- Lesur, G. & Ogilvie, G. I. 2008b, A&A, 488, 451
- Meheut, H., Fromang, S., Lesur, G., Joos, M., & Longaretti, P.-Y. 2015, AA, 579, A117
- Miesch, M. S., Gilman, P. A., & Dikpati, M. 2007, ApJ. Supp. Ser., 168, 337
- Moffatt, H. K. 1977, Magnetic field generation in electrically conducting fluids. (Cambridge University Press)
- Oishi, J. S. & Mac Low, M.-M. 2011, ApJ, 740, 18
- Rincon, F., Ogilvie, G. I., & Proctor, M. R. E. 2007, Phys. Rev. Lett., 98, 254502
- Rincon, F., Ogilvie, G. I., Proctor, M. R. E., & Cossu, C. 2008, Astron. Nachr., 329, 750
- Riols, A., Rincon, F., Cossu, C., et al. 2015, AA, 575, A14
- Riols, A., Rincon, F., Cossu, C., et al. 2013, J. Fluid Mech., 731, 1
- Shi, J.-M., Stone, J. M., & Huang, C. X. 2016, MNRAS, 456, 2273
- Simon, J. B., Hawley, J. F., & Beckwith, K. 2011, ApJ, 730, 94
- Spruit, H. C. 2002, A&A, 381, 923
- Squire, J. & Bhattacharjee, A. 2015, Phys. Rev. Lett., 114, 085002
- Steenbeck, M., Krause, F., & Rädler, K.-H. 1966, Z. Naturforschung Teil A, 21, 369
- Stone, J. M., Hawley, J. F., Gammie, C. F., & Balbus, S. A. 1996, ApJ, 463, 656
- Velikhov, E. P. 1959, Sov. Phys. JETP, 36, 1398
- Walker, J., Lesur, G., & Boldyrev, S. 2016, MNRAS, 457, L39